Unravelling the pre-eruptive conditions of the rhyolitic Šumovit Greben lava dome from clinopyroxene-dominant glomeroporphyritic clots

Kata Molnár, Pierre Lahitte, Boglárka Döncző, Róbert Arató, János Szepesi, Zsolt Benkó, Sébastien Nomade, Jochen Gätjen, Stéphane Dibacto, Marjan Temovski

Contributions to Mineralogy and Petrology (2023) 178:83
https://doi.org/10.1007/s00410-023-02066-0

ORIGINAL PAPER

Unravelling the pre-eruptive conditions of the rhyolitic Šumovit Greben lava dome from clinopyroxene-dominant glomeroporphyritic clots

Kata Molnár[1] · Pierre Lahitte[2] · Boglárka Döncző[3] · Róbert Arató[1,4] · János Szepesi[1,5] · Zsolt Benkó[1,6] · Sebastien Nomade[7] · Jochen Gätjen[8] · Stéphane Dibacto[2,9] · Marjan Temovski[1]

Received: 30 December 2022 / Accepted: 5 October 2023

Abstract

Detailed analyses of mineral composition and whole-rock geochemical data helped to unravel the volcanic plumbing system beneath the rhyolitic Šumovit Greben lava dome, the westernmost member of the Kožuf-Voras volcanic system (N. Macedonia). It is characterized by high SiO_2 content (> 70 wt%) coupled with low MgO (< 1 wt%) and Sr (< 500 ppm) suggesting fractionation of clinopyroxene and plagioclase at depth forming a crystal mush and a crystal-poor rhyolitic lens by fractional crystallization and melt extraction on top of it. The crystal mush is composed of mainly clinopyroxene, biotite and plagioclase, whereas sanidine and plagioclase are the most abundant phenocrysts of the rhyolitic lens. The main dome forming event occurred at ca. 2.9 Ma, which sampled the crystal-poor rhyolitic lens. After a short quiescence time, an explosive eruption occurred depositing a massive lapilli tuff layer northwest of the lava dome, and an extrusion of a small-volume lava flow on the northern side of the lava dome at ca. 2.8 Ma. This latter sampled also the crystal mush, as it contains abundant glomeroporphyritic clots of clinopyroxene ± plagioclase ± biotite. The clinopyroxene phenocrysts are chemically homogeneous, their crystallization temperature is ca. 900 °C representing the crystal mush, whereas the plagioclase and the sanidine crystallized at a lower temperature (ca. 790 °C) representing the rhyolitic lens. Noble gas isotopic composition of the clinopyroxene indicate no mantle-derived fluids (< 0.5%) having an R/R_a of ca. 0.04 R_a. The rejuvenation of the system probably occurred due to implementation of mafic magma at depth leading to a heat transfer and partial melting of the cumulate. This led to crystallization of Ba-rich rims of the sanidine and An- and Sr-rich rims of the plagioclase. The crystal mush zone beneath Šumovit Greben might be connected to the nearby, more mafic volcanic centers, and the eruption of Šumovit Greben could have been the start of the last cycle in the lifetime of the Kožuf-Voras volcanic system.

Keywords Rhyolite · Clinopyroxene · Noble gases · Volcanic plumbing system · Sanidine Ar/Ar dating

Communicated by Timothy L. Grove.

✉ Kata Molnár
molnar.kata@atomki.hu

[1] Isotope Climatology and Environmental Research Centre, HUN-REN Institute for Nuclear Research (ATOMKI), Debrecen, Hungary

[2] GEOPS, CNRS, Université Paris-Saclay, 91405 Orsay, France

[3] Laboratory for Heritage Science, HUN-REN Institute for Nuclear Research (ATOMKI), Debrecen, Hungary

[4] Department of Sedimentology and Environmental Geology, Georg-August University, Göttingen, Germany

[5] MTA-ELTE Volcanology Research Group, Budapest, Hungary

[6] Department of Mineralogy and Geology, University of Debrecen, Debrecen, Hungary

[7] Laboratoire des Sciences du Climat et de l'Environnement, LSCE/IPSL, CEA-CNRS-UVSQ, Université Paris-Saclay, Gif-sur-Yvette, France

[8] Department of Mineralogy and Petrology, Georg-August University, Göttingen, Germany

[9] CNRS, IRD, INRAE, CEREGE, Aix-Marseille Université, 13545 Aix-en-Provance, France

Published online: 27 October 2023

Introduction

Rhyolitic volcanic activity has been witnessed scarcely throughout human history with only a handful of examples in the last century, such as the eruptions of Novarupta-Katmai (USA) in 1912 (Hildreth and Fierstein 2012), Chaitén (Chile) in 2008–2011 (Pallister et al. 2013) and Puyehue-Cordón Caulle (Chile) in 2011–2012 (Castro et al. 2013). These recent examples help to extend our understanding on how the eruption dynamics of these systems work, e.g., the eruption of Chaitén, which highlighted a simultaneous explosive and effusive activity (Carn et al. 2009; Lara 2009; Pallister et al. 2013). However, studying extinct (or seemingly inactive) rhyolitic systems is essential to deepen our knowledge on the pre-eruptive conditions and activation mechanisms.

Rhyolitic volcanism (e.g., Chaos Crag, USA, Hildreth 2007; Kos-Nisyros-Yali, Greece, Bachmann et al. 2012; Rocche Rosse/Lipari, Italy, Bullock et al. 2018; Telkibánya lava dome field, Hungary, Szepesi et al. 2019) is not the dominant type in subduction-related settings, because either their parental magma can erupt before reaching rhyolitic composition or it becomes too crystal-rich to erupt (e.g., Cashman and Blundy 2000; Hildreth 2007; Bachmann and Bergantz 2008). The dominant process in their formation is the fractional crystallization of mafic melts (with some crustal assimilation), which are kept above the solidus temperature by repeated injection of mafic melts in the lower parts of the magma storage system (e.g., Bachmann et al. 2007). The subduction-related rhyolitic volcanism is most often characterized by a cold-wet-oxidized system, where amphibole (and biotite) is the most abundant mafic phase. In contrast, the hot-dry-reduced rhyolites, which occur mostly above mantle upwelling zones, have olivine and pyroxene as the mafic phases (e.g., Bachmann and Bergantz 2008).

Here, we present an example of a subduction-related rhyolitic lava dome (Šumovit Greben, N. Macedonia), which is part of a large volcanic system (Kožuf-Voras) characterized by intermediate (trachyandesitic, trachydacitic and trachytic) volcanic centers (Boev and Yanev 2001). In Šumovit Greben rhyolites, clinopyroxene is the most abundant mafic phase besides biotite (Molnár et al. 2022), which is a rare situation in cold-wet-oxidized systems (Bachmann and Bergantz 2008). By means of geochronology, and detailed textural and mineral chemistry analyses, we aim to unravel the evolution and pre-eruptive conditions of this rhyolitic system highlighting the importance of the clinopyroxene and its relation to the Kožuf-Voras volcanic system. Complemented by noble gas measurements on the main phenocryst phases (sanidine, plagioclase, clinopyroxene), we present a rare example of the applicability of noble gas isotopes in a felsic system.

Geological background

Since the Late Cretaceous times, widespread volcanism, closely linked to the tectonic evolution of the Alpine–Mediterranean region, occurred also in the central part of the Balkan Peninsula. This region is located at the junction of the Dinarides–Hellenides and Carpatho-Balkanides orogens marked by the Sava suture zone, where Africa (Adria)-derived units dominate the western part and Europe-derived units form the eastern part (Fig. 1; Schmid et al. 2020 and references therein). The first peak of magmatism occurred during the Early Oligocene (ca. 33–29 Ma; Boev and Yanev 2001; Lehmann et al. 2013) when large-volume volcanic centers and complexes with mainly calc–alkaline–high-K calc-alkaline geochemical affinity developed in the eastern part of the region (Fig. 1). The second period of volcanism, between ca. 8 Ma and 1.5 Ma (Kolios et al. 1980; Janković et al. 1997; Cvetković et al. 2004; Yanev et al. 2008; Molnár et al. 2022) was restrained to the Vardar zone south of the so-called Skutari-Peć transverse zone (Fig. 1). The SW-vergent fold-and-thrust belt of the Dinarides–Hellenides orogeny is cut by this zone, along which clockwise rotation of the Hellenides belt occurred accelerating in Neogene times due to the back-arc extension in the Aegean region (Handy et al. 2019). This Neogene–recent extension is dominated by NW–SE and E–W trending faults, the latter being linked to the propagation of the North Anatolian fault in the Aegean region at ca. 6 Ma (Dumurdzanov et al. 2005; Burchfiel et al. 2008).

The Late Miocene to Pleistocene small-volume, mafic volcanic centers with high Mg–K and ultrapotassic geochemical characteristics are located at the edges of the extensional basins, along fault zones associated with the boundaries of different tectonic units and nappe structures. These could act as possible pathways for the upwelling magmas from the metasomatized lithospheric mantle (Yanev et al. 2008; Molnár et al. 2022). Contemporary with this spatially scattered magmatism, the Kožuf-Voras volcanic system developed at ca. 6.5–1.8 Ma extending in SW–NE direction along the Macedonian–Greek border (Kolios et al. 1980; Janković et al. 1997; Molnár et al. 2022). It represents the northmost subduction-related system in the region with high-K calc–alkaline–shoshonitic geochemical affinity. The eruption centers of the system developed in time towards the southwest coupled with an increase in K-content of the erupted magmas (Vougioukalakis 1994; Molnár et al. 2022).

The rhyolitic Šumovit Greben is the westernmost lava dome of the Kožuf-Voras volcanic system, which formed at ca. 2.9–2.8 Ma (Molnár et al. 2022). It is located at the eastern edge of Mariovo basin between Kozjak and Nidže Mts (Fig. 2). The formation of the lava dome structure consists of two phases starting with a lava dome extrusion at ca.

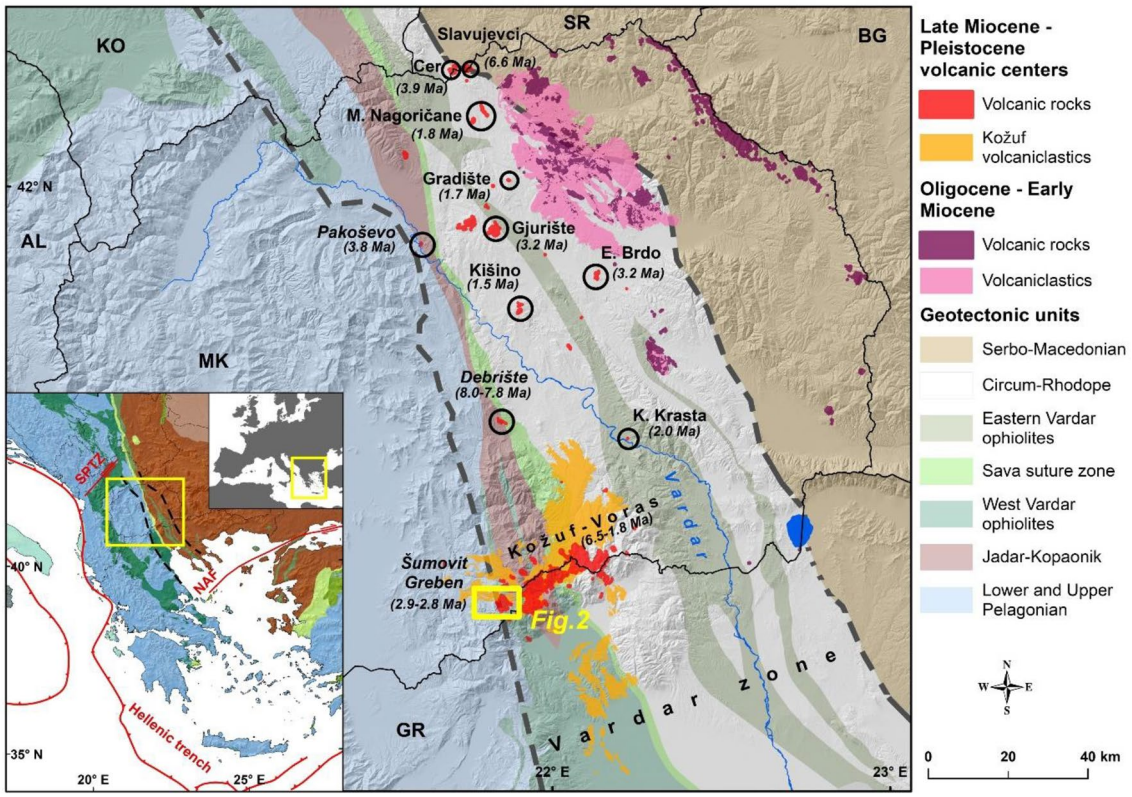

Fig. 1 Geological map of the study area modified after Schmid et al. (2020). Circles mark the localities of the Late Miocene to Pleistocene centers with known eruption age (Kolios et al. 1980; Janković et al. 1997; Cvetković et al. 2004; Yanev et al. 2008; Molnár et al. 2022). Grey dashed lines indicate the extent of Vardar zone. SPTZ: Skutari-Peć transverse zone; NAF: North Anatolian Fault

2.9 Ma producing the main volume of the center. Different lithofacies of a slowly cooling rhyolitic dome (i.e., basal breccia, coherent glass, foliated rhyolite and microcrystalline rhyolite; Manley and Fink 1987) are present at different parts of the volcanic center (Figs. 2, 3). Parts of the basal breccia are altered, hydrated to perlite being in the focus of past mining activity. Remnants of a neck/feeder dyke mark the potential conduit(s) for the upwelling magmas. A small-volume lava flow, restricted only to the northern part of the center, marks the end of activity at ca. 2.8 Ma. In addition, a massive lapilli tuff layer crops out along roadcuts northwest from Šumovit Greben (Fig. 2).

This study focuses on the 2.8 Ma lava flow (remnant), which contains abundant clinopyroxene ± plagioclase ± biotite glomeroporphyritic clots, possibly representing a deeper, crystal mush zone of the volcano plumbing system. We applied detailed mineral chemistry on selected phases to constrain the temperature and depth of the crystal mush, complemented with noble gas isotopic analyses to decipher the evolution of the system. In addition, we aim to characterize in more detail the ambiguous relation between the massive lapilli tuff unit and the lava dome by applying whole-rock geochemistry and sanidine $^{40}Ar/^{39}Ar$ dating.

Samples and analytical methods

We conducted a field campaign during the summer of 2019 and 2021 to collect suitable samples from every mapped unit, i.e., fresh, unaltered, large blocks. A detailed map of the area was presented in Molnár et al. (2022), while an updated map of all the sampled localities is presented in Fig. 2. An additional sample was collected from a ca. 3 m thick, massive lapilli tuff layer (ignimbrite; SG01), which crops out along a roadcut northwest from the lava dome. It is an unsorted, non-welded, matrix-supported layer containing crystal-poor pumices (up to 7 cm in size) and scarce lithic clasts (< 5 cm).

General petrography and whole-rock geochemistry

Petrography of the studied samples was performed by combined investigation of a petrographic microscope (Olympus BX53 equipped with Olympus DP23 camera) and a JEOL JSM-IT500HR type SEM equipped with a JEOL EX-74232U1L4Q type EDS detector and a Centaurus CL detector at the Institute for Nuclear Research (Atomki), Debrecen, Hungary.

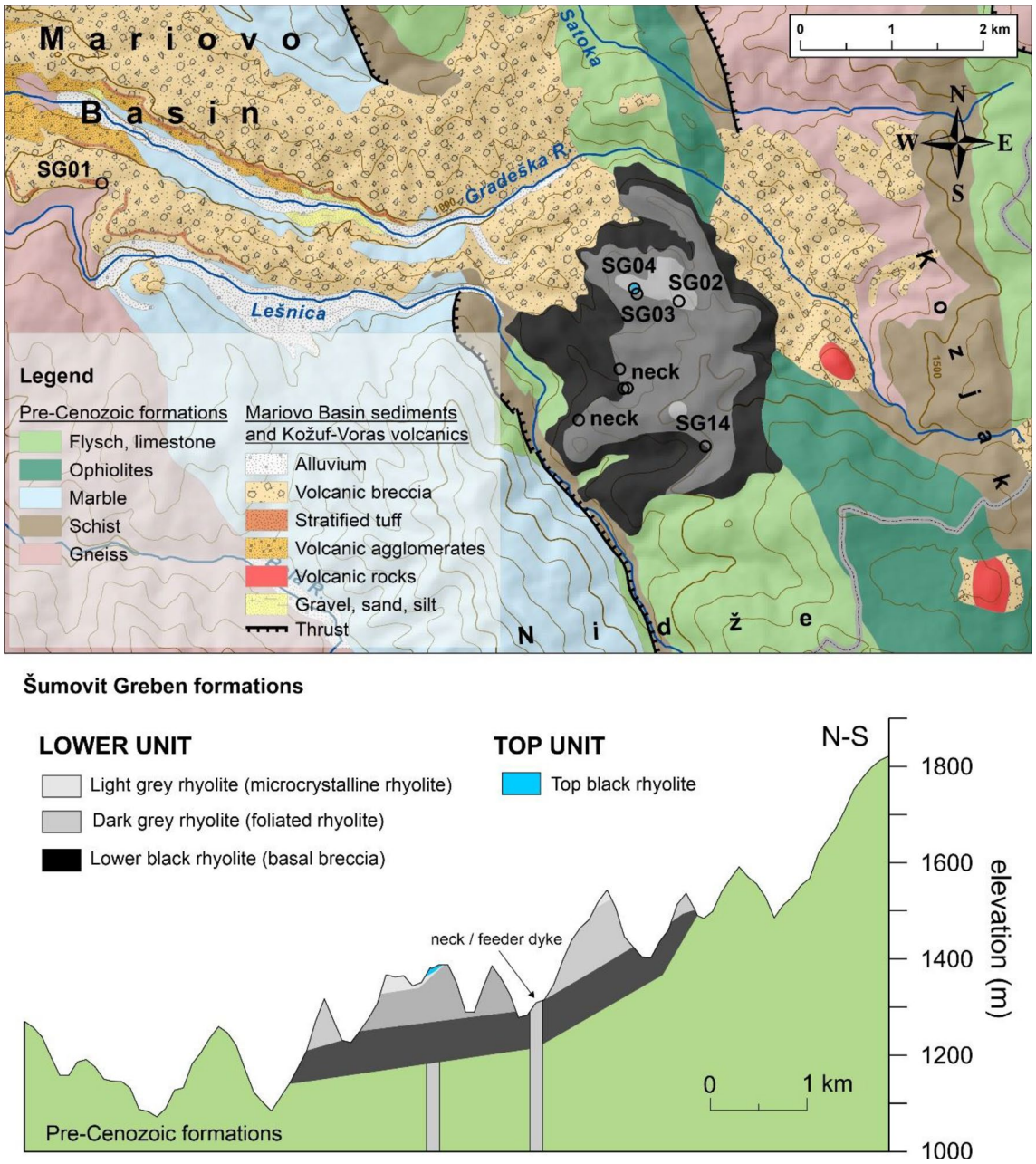

Fig. 2 Geological map and an N–S cross section of Šumovit Greben lava dome. Circles mark the location of the mentioned samples (modified after Molnár et al. 2022)

Whole-rock major and trace element geochemical composition of pumices from the ignimbrite unit (SG01) were analyzed at AcmeLabs (Vancouver, Canada; http://acmelab.com). Major and minor elements were determined by ICP-emission spectrometry, whereas trace elements were analyzed by ICP–MS following a lithium–borate fusion and dilution in acid.

Mineral chemistry

Electron microprobe analyses for in-situ mineral chemistry of the phenocryst assemblages (pyroxene, feldspar, glass inclusions) were performed at the Goettingen laboratory for correlative Light and Electron Microscopy (GoeLEM) of the Georg-August University Göttingen using a JEOL

Fig. 3 Field photographs of the different lithofacies at Šumovit Greben volcanic center. **a** Massive lapilli tuff layer along the roadcut northwest from the lava dome (SG01). **b** Folding along a flow front in the dark grey rhyolite. **c** Remnant of a neck/feeder dyke with vertical foliation. **d** Hand specimen from the top black, glassy rhyolite (SG04) with feldspar (fs) phenocrysts. **e** Outcrop of the lower black rhyolite with the dark grey rhyolite of the lower unit, their boundary is marked with red dashed line. **f** Close-up view on the lower black rhyolite (SG14)

JXA-iHP200f EPMA. The instrument is equipped with a Schottky field emitter and five spectrometers for wavelength-dispersive X-ray spectrometry (WDS). All quantitative measurements were performed at an acceleration voltage of 15 kV and a beam current of 15 nA. For calibration, we used natural (albite: Na; anorthite: Al, Si, Ca; celsian: Ba; hematite: Fe; olivine: Mg, Si; rhodonite: Mn; sanidine: K; topas: F; wollastonite: Ca) and synthetic (Cr_2O_3:Cr; NiO:Ni; $ScPO_4$:P; $SrTiO_3$:Sr; TiO_2:Ti) reference materials. The measurement conditions including element selection were adapted to the matrix type. For analyses of pyroxene, we used a beam diameter of 5 µm and counting times of 15 s (Na, Mg, K, Ca, Al, Si, Fe) and 30 s (Ti, Cr, Mn, Ni) on the characteristic X-ray lines. For analyses of feldspar, we used a beam diameter of 20 µm and counting times of 15 s (Na, Al, Si, K, Ca) and 30 s (Fe, Sr, Ba). For analyses of the glass inclusions, we used a beam diameter of 10 µm or smaller depending on the size of the inclusions and counting times of 15 s (Na, Mg, Al, Si, K, Ca, Fe), 30 s (Ti, Cr, Mn, Ni, Sr, Ba) and 60 s (F, P). For measuring Si and Ca, we switched between the calibrations performed on the reference materials olivine and wollastonite (pyroxene) and anorthite (feldspar and glass inclusions). Matrix correction was applied using the phi-rho-z algorithm of the XPP method by Pouchou and Pichoir (1991). Analytical errors and detection limits were calculated from the counting statistics of peak and background signals, following the Gauss law of error propagation. Detailed measurement conditions and results are presented in the Supplementary Material.

Noble gas isotopic analyses

Clinopyroxene, sanidine and plagioclase crystals were separated from the samples SG04 and SG14. 0.4 to 1.8 g of pure crystal separates (250–500 µm) were cleaned in acetone in ultrasonic bath, loaded into stainless-steel holders with a magnetic ball and baked at ca. 100 °C for 24 h in vacuo before the analyses. Noble gases were measured at the Isotope Climatology and Environmental Research Centre (ICER Centre), Atomki. The gases were released by single-step crushing (150 strokes), purified and separated by a cryogenic trap. Helium and neon abundances were measured on an HELIX–SFT and a VG-5400 mass spectrometers, respectively. Faraday detector was used for ^{4}He, whereas ^{3}He and all Ne isotopes were measured on electron multipliers. Detailed description of the analytical procedures can

be found in Papp et al. (2012) and Molnár et al. (2021a). Blank levels are 5×10^{-11} and $0.9–1 \times 10^{-10}$ ccSTP/g for He and Ne, respectively (ccSTP: cubic centimeter at standard temperature and pressure, 0 °C and 1 atm).

$^{40}Ar/^{39}Ar$ dating

Sanidine crystals (250–500 µm) were separated from the massive lapilli tuff unit (SG01) at the ICER Centre, Atomki for $^{40}Ar/^{39}Ar$ dating. Twenty fresh and transparent K-rich feldspars were handpicked and irradiated in the Cd-lined core CLICIT facility of the Oregon State University TRIGA reactor for 2 h. Following irradiation, measurements were performed at the Laboratoire des Sciences du Climat et de l'Environnement (CEA, CNRS UMR, France) dating facility. Gases of 11 crystals were individually extracted by fusion using a CO_2 laser and purified using 3 SAES getters. Before fusion, each crystal underwent a sweeping to remove unwanted gas potentially trapped on the crystals. The five argon isotopes (i.e., ^{40}Ar, ^{39}Ar, ^{38}Ar, ^{37}Ar, and ^{36}Ar) were measured using a multi-collector NGX 600 mass spectrometer. In a first run, ^{40}Ar, ^{39}Ar, and ^{38}Ar were measured simultaneously on 3 ATONA® amplifiers and ^{36}Ar on the electron multiplier. Next, the ^{37}Ar was measured alone using the electron multiplier. Neutron fluence J factor ($0.0005591 \pm 0.000000335$) was calculated using co-irradiated Alder Creek sanidine standard (ACs-2; 1.1891 Ma; Niespolo et al. 2017) according to the K total decay constant of Renne et al. (2011; $\lambda_{e.c.} = (0.5757 \pm 0.016) \times 10^{-10}$ year^{-1} and $\lambda_{\beta^-} = (4.9548 \pm 0.013) \times 10^{-10}$ year^{-1}). Discrimination is calculated according to the $^{40}Ar/^{36}Ar$ ratio of 298.56 (Lee et al. 2006). Procedural blank measurements, typically $2.1–2.3 \times 10^{-4}$ V for ^{40}Ar and $7.8–7.9 \times 10^{-7}$ V for ^{36}Ar, were achieved after every two to three unknowns. Full analytical data for each sample and detailed description of the analytical procedures can be found in the Supplementary Materials.

Results

Petrography and geochemistry

Whole-rock geochemical data were already reported by Molnár et al. (2022) for the Šumovit Greben lava rocks, characterized as rhyolites belonging to the (high-K calc–alkaline)–shoshonitic series (Fig. 4; Peccerillo and Taylor 1976). The sampled ignimbrite layer (SG01) has rhyolitic composition similar to the Šumovit Greben lava rocks, with elevated K content (71.4 wt% SiO_2; 6.5 wt% K_2O; recalculated anhydrous) together with the low MgO (< 1 wt%) and Sr (240 ppm) content (Fig. 4; Supplementary Materials).

The lower (older) unit consists the lower black rhyolite (basal breccia; SG14), the dark grey rhyolite (foliated rhyolite; SG03) and the light grey rhyolite (microcrystalline rhyolite; SG02; Fig. 2) It has a phenocryst assemblage of K-feldspar, quartz, plagioclase, biotite, clinopyroxene and scarce amphibole along with titanite, Fe–Ti oxides, apatite and zircon as accessory phases. K-feldspar and plagioclase form occasionally glomeroporphyritic clots. The crystallinity of the groundmass depends on the differential cooling rate of the unit showing glassy groundmass with perlitic texture and foliation closer to the bottom of the unit, and devitrified and glassy textures in the middle section. The top (younger) unit is a massive, black rhyolite with glassy groundmass and perlitic texture (SG04; Fig. 2). Its mineral assemblage is similar to the bottom unit with a large number of clinopyroxene ± plagioclase ± biotite glomerocrysts (Fig. 5) in addition to the K-feldspar + plagioclase clots.

The sample from the massive lapilli tuff unit (SG01) shows similar mineral assemblage to the lava rocks. It is a crystal- and clast-poor matrix-supported (ash) unit with pumices and crystal fragments (Fig. 5) containing K-feldspar, plagioclase, biotite and clinopyroxene as the dominant phenocrysts and Fe–Ti oxide, titanite, apatite and zircon as accessory phases.

The whole-rock composition of the massive lapilli tuff sample shows similar trend but slightly depleted character both in rare earth (REE) and in trace elements compared to the lava rocks of Šumovit Greben (Fig. 4; Suppl. Mat.). It has a negative Eu-anomaly, and a U-shaped middle-to-heavy REE pattern characteristic for wet-oxidized rhyolites (Bachmann and Bergantz 2008). Similar to the lava rocks, the massive lapilli tuff sample shows enrichment in large-ion lithophile elements (except Ba), U and Th relative to some of the high-field-strength elements (Nb, Ti), Sr and P (Fig. 4).

Mineral chemistry

The Šumovit Greben rhyolites contain both K-feldspar and plagioclase as phenocrysts. The K-feldspar occurs mainly as euhedral–anhedral single crystals in a size of ca. 200 µm to 2.5 mm; however, crystals with slightly rounded corners are also present, dominantly in the top unit (Fig. 5). In addition, the K-feldspar seldom forms glomeroporphyritic clots with plagioclase present in both units (Fig. 5). Their overall composition is mainly sanidine varying in the range from Or_{47} to Or_{61} in the lower unit and from Or_{35} to Or_{64} in the top unit (Fig. 6).

It occasionally shows normal, reverse and step zonation related to changes in Ba (and in lesser extent Sr) content, most abundantly in the top lava unit (SG04; Fig. 5). Few crystals in the lower unit can be described as anorthoclase ($Or_{17–22}$; Fig. 6). The sanidine crystals show differences in their BaO content between the units: it can be up to 4.5

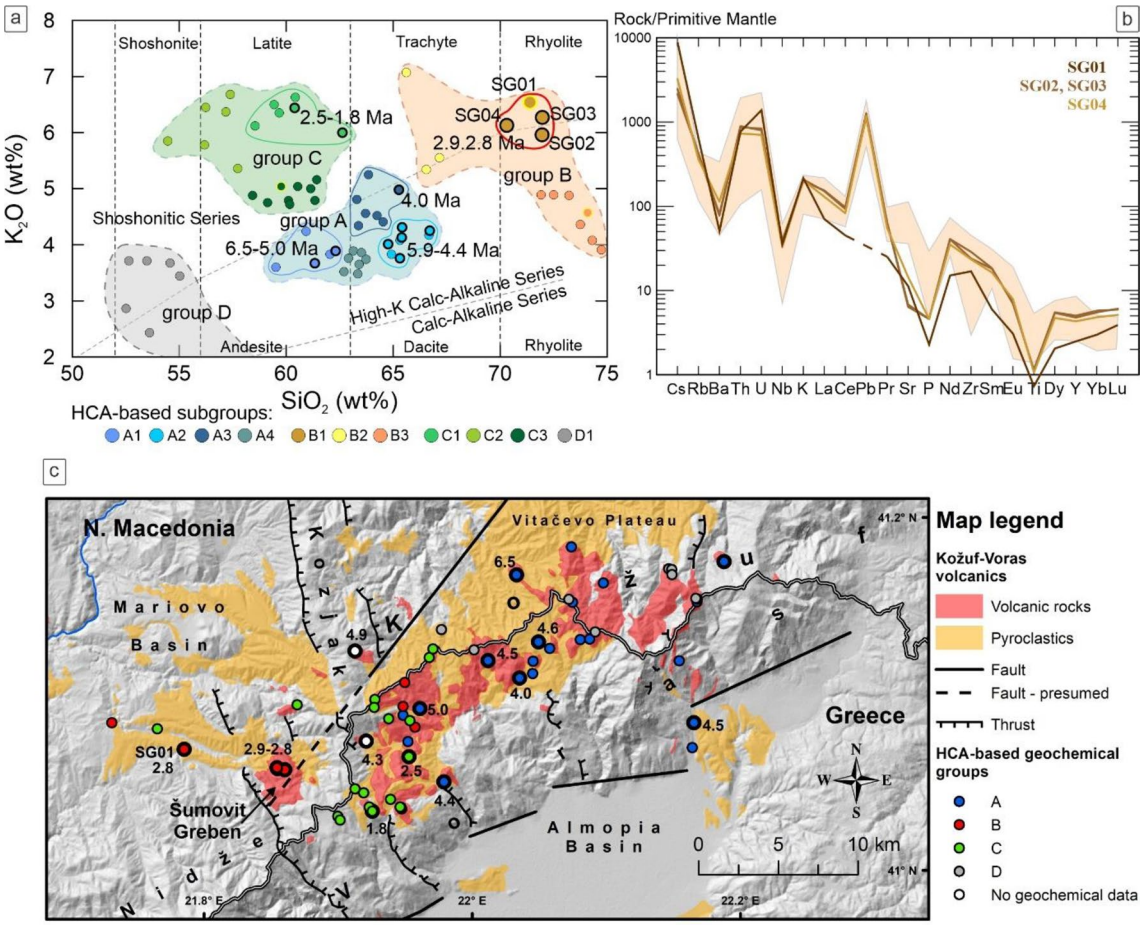

Fig. 4 Whole-rock major and trace element characteristics of Kožuf-Voras volcanic field. **a** SiO_2 vs. K_2O diagram (Peccerillo and Taylor 1976) with the hierarchy cluster analyses (HCA)-resulted groups modified after Molnár et al. (2022). Eruption age intervals are marked for each subgroup (Kolios et al. 1980; Janković et al. 1997; Molnár et al. 2022). Šumovit Greben samples are marked by red outline. **b** Primitive-mantle normalized trace element plot (Sun and McDonough 1989) of the analyzed Šumovit Greben samples (Molnár et al. 2022 and this study). The trace element characteristics of Kožuf-Voras volcanic field are presented in the background. **c** Spatial distribution of the lava domes of Kožuf-Voras volcanic system, color coded according to the HCA-groups (modified after Molnár et al. 2022). Localities with known eruption ages are marked with thick black outlines

wt% in the top unit, whereas it remains below 0.2 wt% in the lower unit (Fig. 6). Similar variation can be observed in their SrO content, although to a lesser extent. Plagioclase is mainly present as anhedral phenocryst in a size of ca. 150 µm to 2.5 mm, and also as part of glomeroporphyritic clots with K-feldspar in both units and with clinopyroxene ± biotite in the top unit (Fig. 5). The plagioclase composition ranges from An_{17} to An_{70} in the top unit showing patchy, normal zonation and spongy texture occasionally, and a narrower compositional range (An_{14}–An_{25}) in the lower unit (Fig. 6). Those in the glomeroporphyritic clots with clinopyroxene range between An_{20} and An_{48} (Fig. 6). The Sr content of the plagioclase show a positive correlation with the An content in both units. The FeO content is fairly homogeneous in the lower unit (~0.25 wt%), whereas it has a range of 0.15–0.86 wt% in the top unit with the higher values found in the aggregates (Fig. 6).

Clinopyroxene is an abundant mafic mineral in the studied units, especially in the top lava unit (SG04), where it forms glomerocrysts with ± plagioclase ± biotite with a size of ca. 700 µm to 3.5 mm. It contains inclusions of Fe–Ti oxide, apatite, zircon, titanite and glass (Fig. 5). The phenocrysts occur as euhedral–anhedral crystals with a size of ca. 150 µm to 1 mm showing uniform composition of ferro-diopside–(Mg-rich) augite with a narrow range of variation in the FeO and MgO content (Fig. 6) and an average Mg#-number of 68 ± 1 for both units. The clinopyroxene-hosted glass inclusions have rhyolitic composition, similar to the whole-rock composition of the lava rocks (SiO_2 = 71.9 ± 2.6 wt%, K_2O = 7.0 ± 2.3 wt%; Figs. 6, 9).

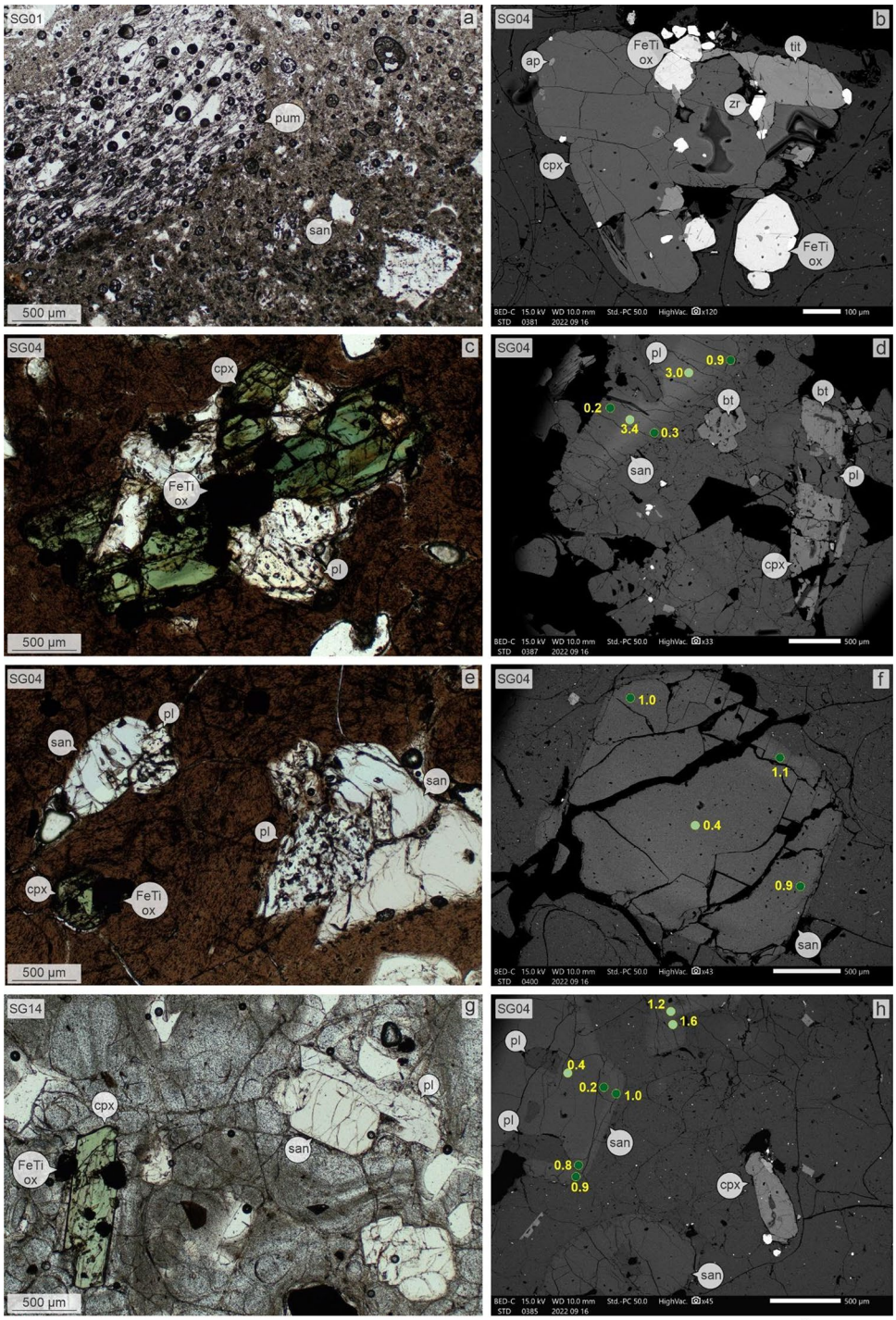

Fig. 5 Petrographic microscope (**a**, **c**, **e**, **g**) and SEM–BSE images (**b**, **d**, **f**, **h**) of Šumovit Greben samples. BaO contents (in wt%) in the sanidine cores and rims are marked with pale and dark green circles, respectively. **a** Representative petrographic image of the crystal-poor SG01 ignimbrite sample with pumice (pum) and sanidine (san) fragments. **b** SEM–BSE image of a clinopyroxene (cpx) cluster with zoned titanite (tit), Fe–Ti oxide (FeTiox), zircon (zr) and apatite (ap) as inclusions. **c** Representative petrographic image of clinopyroxene–plagioclase (pl) glomeroporphyritic clot in sample SG04. **d** SEM–BSE image of a normal zoned sanidine crystal intergrown with plagioclase together with biotite (bt) and clinopyroxene from sample SG04. **e** Representative petrographic image of sanidine–plagioclase and clinopyroxene–Fe–Ti oxide glomeroporphyritic clots in sample SG04. Note the spongy texture of the plagioclase and the slightly rounded corner of the sanidine. **f** SEM–BSE image of an individual sanidine phenocryst with step zonation. **g** Representative petrographic image of sample SG14 with clinopyroxene phenocryst, sanidine and plagioclase. **h** SEM–BSE image of sanidine with plagioclase inclusion and a clinopyroxene in sample SG04. Note the rounded shape of the individual sanidine

Noble gas isotope systematics

We determined the He and Ne composition of the fluid inclusions hosted in clinopyroxene, sanidine and plagioclase phenocrysts from the lowermost (SG14) and top (SG04) lava rock units. The results are presented in Fig. 7 and Supplementary Materials.

The clinopyroxene separates show a higher concentration of noble gases than the sanidine and plagioclase. Their helium and neon concentrations vary between 2.8–4.1 × 10^{-8} ccSTP/g and 1.4–2.7 × 10^{-10} ccSTP/g, respectively. In the sanidine and plagioclase separates, helium and neon concentrations are very close to the instrumental detection limits varying between 0.5–1.2 × 10^{-9} ccSTP/g and 0.9–2.0 × 10^{-10}

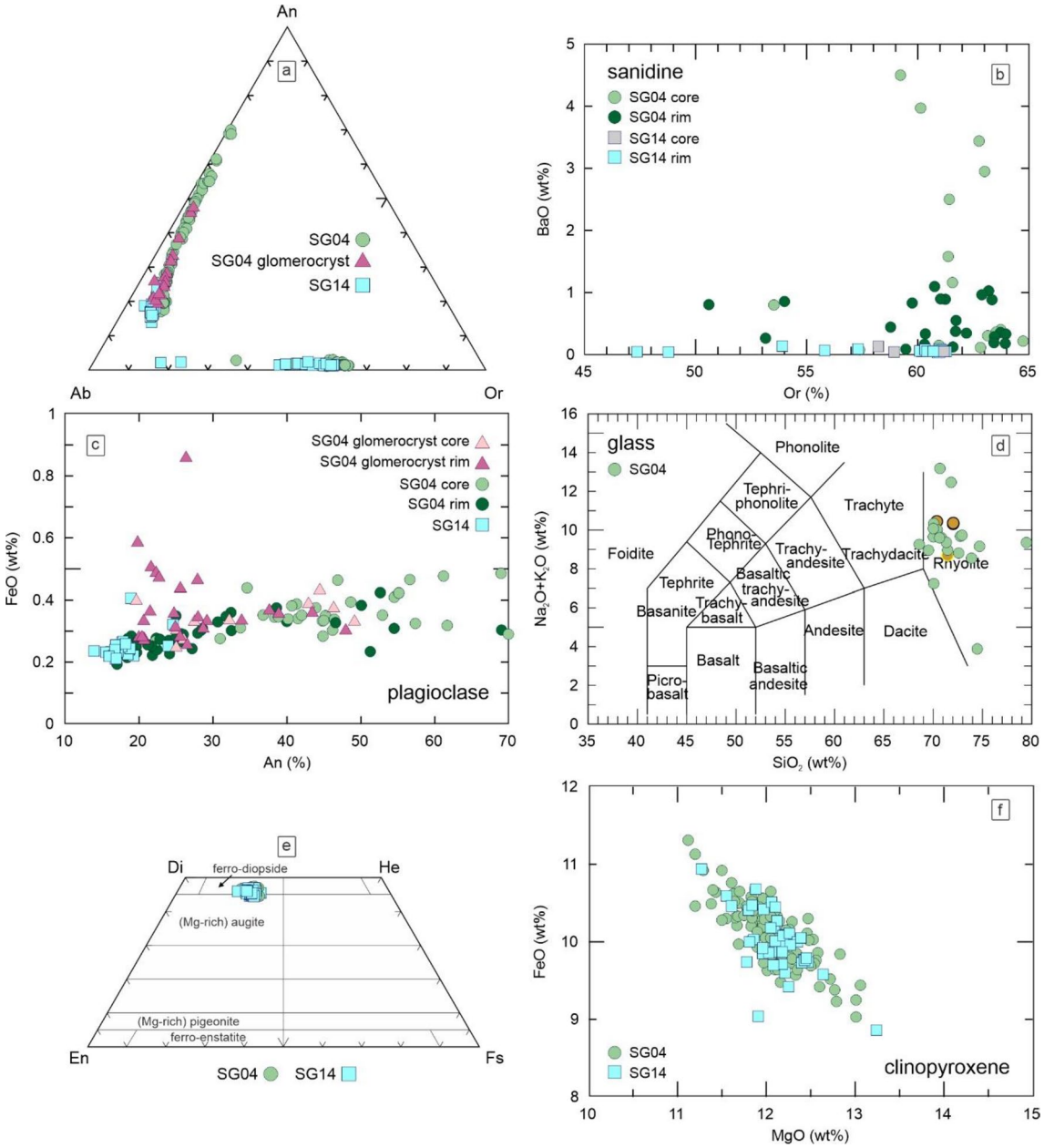

Fig. 6 Chemical composition of the different phases in the lower (SG14) and top (SG04) lava units. **a** Composition of feldspar phenocrysts based on the anorthite(An)–albite(Ab)–orthoclase(Or) triangle. **b** BaO (wt%) vs. the orthoclase (%) content of the sanidine phenocrysts. **c** FeO (wt%) vs. the anorthite (%) content of the plagioclase phenocrysts and glomerocrysts. **d** Composition of the clinopyroxene-hosted glass inclusions according to the total alkali silica (Le Bas et al. 1986) diagram; whole-rock composition of Šumovit Greben samples is marked with brown circles. **e** Composition of the clinopyroxene phenocrysts based on the diopside(Di)–hedenbergite(He)–enstatite(En)–ferrosilite(Fs) quadrilateral (Morimoto et al. 1988). **f** FeO (wt%) vs. MgO (wt%) variation of the clinopyroxene phenocrysts

ccSTP/g, respectively. The R/R_a ratios (where R is the $^3He/^4He$ ratio of the sample and R_a is $(1.382 \pm 0.005) \times 10^{-6}$; Sano et al. 2013) of the clinopyroxene separates from the top unit range at around 0.03 R_a, whereas their $^4He/^{20}Ne$ ratios vary between 100 and 300 showing no or negligible (< 0.5%) sign of atmospheric contamination. Clinopyroxene separate from the bottom unit exhibits similar $^4He/^{20}Ne$ ratio but lower R/R_a value compared to the top unit clinopyroxene (Fig. 7).

$^{40}Ar/^{39}Ar$ age of the massive lapilli tuff layer

$^{40}Ar/^{39}Ar$ dating results of the SG01 sample are presented in Fig. 8 together with the corresponding Kernel density

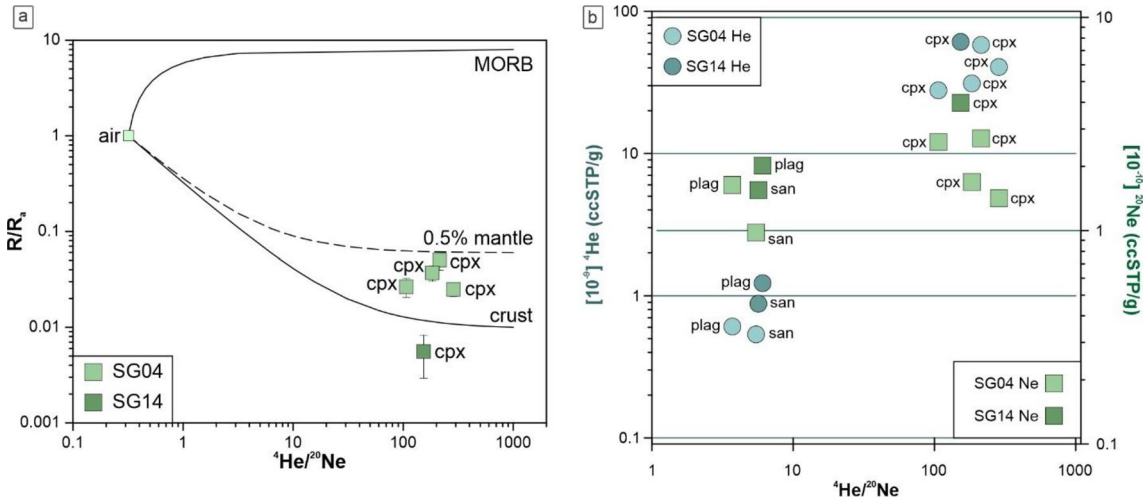

Fig. 7 Noble gas isotopic systematics of the studied mineral phases. A. R/R_a vs. $^4He/^{20}Ne$ plot. B. ^4He and ^{20}Ne concentrations vs. the $^4He/^{20}Ne$ ratios with their uncertainties (equivalent with the size of the rectangle/circle unless marked otherwise). The measured separates are clinopyroxene (cpx), sanidine (san) and plagioclase (plag) from the bottom (SG14) and top (SG04) lava unit. Assumed end-members in the R/R_a vs. $^4He/^{20}Ne$ plot: atmospheric (1 R/R_a, 0.318 $^4He/^{20}Ne$; Sano and Wakita 1985), crustal (0.02 R/R_a, 1000 $^4He/^{20}Ne$; Sano and Marty 1995) and MORB (8 R/R_a, 1000 $^4He/^{20}Ne$; Graham 2002)

estimates. Weighted mean age uncertainties are reported at 2σ, including J uncertainty, calculated using Isoplot 4.0 (Ludwig 2012). Despite the low spread of the Inverse isochron, the resulting $^{40}Ar/^{36}Ar$ initial intercepts is within uncertainty of that of the atmosphere suggesting that the dated sanidine crystals do not contain trapped excess argon. Nine out of the eleven analyzed single crystal display statistically identical age and were, therefore, used to calculate a weighted mean age. The two other older crystals, 4.27 ± 0.02 and 2.94 ± 0.02 Ma, are interpreted as xenocrysts. The main population of crystals is interpreted as juvenile, with weighted mean age of 2767 ± 7 ka (15 ka, including all uncertainties, MSWD = 0.72, $p = 0.67$). This age is hereafter interpreted as the age of deposition of this volcanic unit.

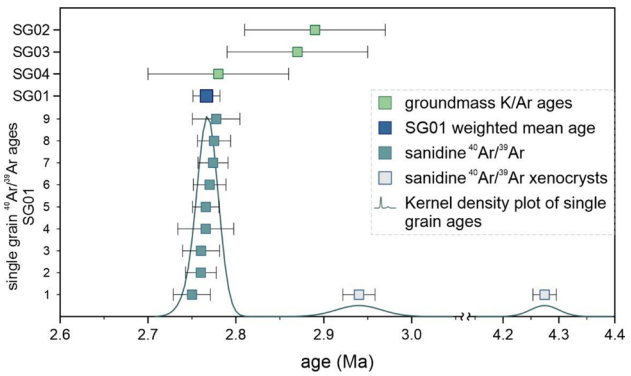

Fig. 8 Combined sanidine $^{40}Ar/^{39}Ar$ and groundmass K/Ar ages (Molnár et al. 2022) with 2σ uncertainties from Šumovit Greben ignimbrite (SG01) and lava rocks (SG02, SG03, SG04). The Kernel density estimate was plotted from the single grain sanidine $^{40}Ar/^{39}Ar$ ages (Vermeesch 2012)

Discussion

Formation of Šumovit Greben lava dome

The internal structure and different lithofacies of a rhyolitic lava dome or lava flow has long been described at several examples worldwide (e.g., Little Glass Mountain, USA; Fink 1983; Obsidian Dome, USA; Manley and Fink 1987; Rocche Rosse, Italy; Bullock et al. 2018; Telkibánya Lava Dome Field, Hungary; Szepesi et al. 2019). Rhyolitic lava domes consist (from bottom to top) of units/layers of basal breccia, thinner obsidian, foliated rhyolite, thick obsidian and an upper/carapace breccia (e.g., Manley and Fink 1987). In addition, different deformation processes had been identified resulting in diverse disruption in foliation and additional folding as the flow advances (e.g., Fink 1983; Bullock et al. 2018). Although highly affected by erosion and perlite alteration, several of these lithofacies and features can be recognized at Šumovit Greben. Its lowermost unit is a basal breccia (entirely hydrated to perlite at several places; SG14) followed by a foliated and a massive rhyolite (SG02, SG03; Figs. 2, 3). Large scale folding, due to progressive deformation (e.g., Flinn 1962; Ramsay 1979; Bullock et al. 2018), can be observed along some of the flow fronts (especially in the northern section; Fig. 3). Based on groundmass K/Ar ages, the main lava dome formed at ca. 2.89–2.87 ± 0.08 Ma (Fig. 7; Molnár et al. 2022). The

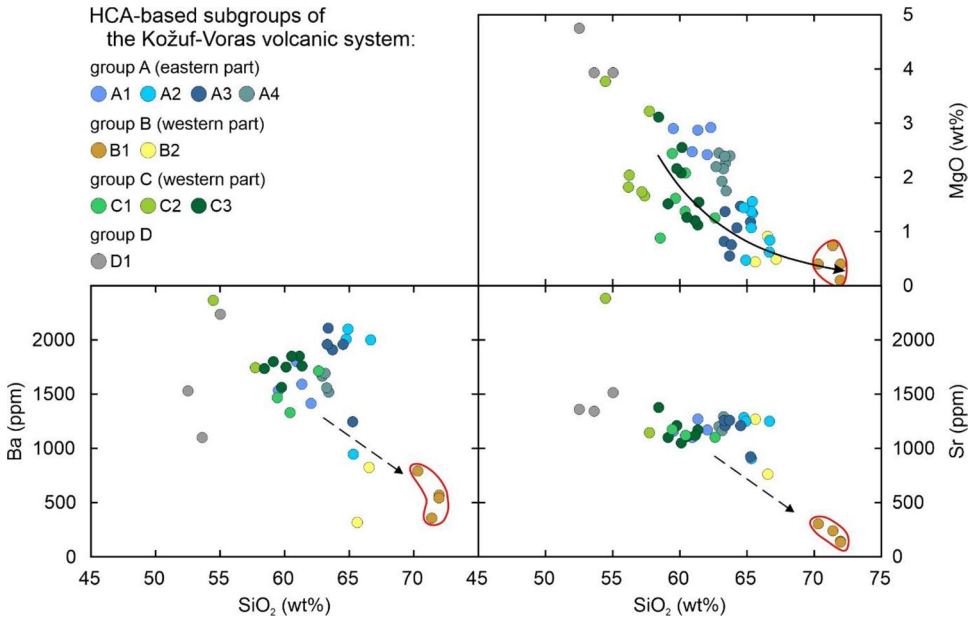

Fig. 9 Selected major and trace element compositions of magmas from the Kožuf-Voras volcanic system with the HCA-groups modified after Molnár et al. (2022). Šumovit Greben samples are outlined in red in each panel. A possible fractional crystallization path is plotted on the MgO vs. SiO_2 diagram having group C magmas as a theoretical starting composition (black solid line). Note the decrease in Ba and Sr content (highlighted by black intermittent lines) in the Šumovit Greben samples compared to the other samples in the volcanic system as a result of fractional crystallization and melt extraction

low phenocryst content, together with the low MgO and Sr content (Fig. 9) suggest extensive plagioclase and pyroxene crystallization at a deeper part of the magma storage, and indicate that the lava dome forming eruption was fed by a crystal-poor rhyolitic lens. The rhyolitic lens is most likely formed by fractional crystallization and melt extraction from a crystal mush of intermediate composition, i.e., a silicic cumulate (e.g., Deering and Bachmann 2010). This is supported by the low MgO, Sr, Ba content and Zr/Hf ratio of the erupted high-silica ($SiO_2 > 70$ wt%) magmas (Fig. 9). The topmost rhyolitic unit (SG04), which crops out only at a restricted area could represent the carapace breccia of the lava dome completing the lithofacies succession. However, this unit displays slightly distinct petrological and geochemical characteristics compared to samples from the lower units. It contains a large number of glomeroporphyritic clots of clinopyroxene ± plagioclase ± biotite, which are lacking in the other samples. It displays lower SiO_2 (Figs. 4, 6, 9) and slightly higher MgO content (Fig. 9), slightly higher $^{143}Nd/^{144}Nd$ and lower $^{87}Sr/^{86}Sr$ ratios compared to the main lava dome (Molnár et al. 2022). These characteristics imply that even though this unit was also fed by the rhyolitic lens, it has also tapped the crystal mush, a slightly deeper part of the magma storage system. Groundmass K/Ar ages suggest slightly younger eruption age than the underlying unit (2.78 ± 0.08 Ma; Fig. 8; Molnár et al. 2022). Although the age overlaps within uncertainties with the lower units, the different petrological and geochemical features, and the slightly younger age imply that the topmost unit can be interpreted as a separately extruded small lava flow towards the end of the volcanic activity.

The volcanic activity at Šumovit Greben was characterized by additional explosive eruption, as also seen at the rare recent examples of rhyolitic eruptions (e.g., Mono-Inyo Craters, USA; Sieh and Bursik 1986; Chaitén volcano, Chile; Carn et al. 2009). The petrological and geochemical characteristics of the massive lapilli tuff (ignimbrite) unit show strong similarities to the lava rock samples having a rhyolitic composition, together with the low MgO (< 1 wt%) and Sr (< 300 ppm) content (Fig. 9), which imply these rocks erupted from a very similar source/volcanic center. This is further supported by sanidine $^{40}Ar/^{39}Ar$ geochronology revealing that the eruption age of the ignimbrite unit is 2.77 ± 0.02 Ma (Fig. 8). As it closely overlaps within uncertainty with the top unit, it is difficult to decipher the order of events. One of the possibilities is that the explosive eruption followed the extrusion of the top unit, which might have been a larger lava flow mainly destroyed by the explosive eruption (together with the top part of the bottom unit). The other possibility is that the explosive eruption slightly preceded the extrusion of the top lava unit. Such a sequence might be supported by the lack of carapace breccia in the main lava dome, which could have been destroyed by the explosive eruption.

In addition, the greater involvement of the crystal mush in the top unit (based on the abundance of clinopyroxene aggregates) implies that the size/contribution of the crystal-poor lens possibly decreased, as a combined result of the lava dome formation (bottom unit) and the explosive eruption (depositing the ignimbrite unit). The example of the Chaitén eruption shows renewal of volcanic activity starting with a large explosive eruption and following a lava dome forming phase (e.g., Carn et al. 2009; Lara 2009). A similar scenario could have occurred during the second stage of volcanic activity at Šumovit Greben following the main lava dome building phase (ca. 2.9 Ma). After ca. 100 ka of quiescence,

the renewal possibly started with a large explosive eruption destroying the topmost parts of the previously formed lava dome. It was shortly followed by the extrusion of a small-volume lava flow, i.e., the top unit of the lava dome.

Pre-eruptive conditions of the volcanic plumbing system

The presence of clinopyroxene in rhyolite is relatively common, especially in case of hot-dry-reduced magmas (Bachmann and Bergantz 2008), such as the Yellowstone rhyolites (e.g., Ellis and Wolff 2012; Ellis et al. 2014; Troch et al. 2017). However, the occurrence of clinopyroxene in cold-wet-oxidized magmas, i.e., in subduction-related settings is scarcer (e.g., Hildreth and Fierstein 2012). The main mafic phenocryst in the Šumovit Greben rhyolites is clinopyroxene offering a unique insight to study its influence on the volcanic plumbing system and the pre-eruptive conditions.

The petrological and geochemical features of the studied rocks imply that the volcanic plumbing system is composed of a deeper crystal mush, where mainly clinopyroxene and plagioclase fractionation took place and the rhyolitic crystal-poor lens formed on top of it. This is supported by the extremely low MgO content of the whole-rock samples (< 1%, in some cases below detection limit) and the low Sr content (< 300 ppm). The eruptions sampled mainly the overlying rhyolitic lens to different extent. The larger amount of clinopyroxene phenocrysts, abundant glomeroporphyritic clots of clinopyroxene ± plagioclase ± biotite, and slightly different geochemical features of the top lava flow imply that in the last eruption, the underlying crystal mush zone was involved to some extent as well. The detailed mineral chemistry measurements displayed no compositional differences neither between the clinopyroxene phenocrysts from the lower and the top unit, nor between the phenocrysts and aggregates within the top unit. The clinopyroxene crystals are ferro-diopside–(Mg-rich) augite in composition exhibiting a narrow range in their FeO (8.9–11.3 wt%) and MgO (11.1–13.2 wt%) content (Fig. 6). This implies that no large-scale re-equilibration took place prior to the eruption.

Crystallization temperatures calculated from clinopyroxene single crystals using the R-based random forest machine learning of Higgins et al. (2021), were in a uniform range of 905 ± 8 °C (standard deviation of $n = 161$, the uncertainty of the method is ca. 30 °C; Supplementary Material), independently of the samples or types of crystals (i.e., phenocrysts or part of the crystal aggregates). Using the same method, the crystallization pressure was estimated at 5 ± 1 kbar (s.d. of $n = 161$, the uncertainty of the method is 3 kbar; Supplementary Material), equivalent to a depth of approximately 15 ± 3 km. However, recent studies highlighted the high uncertainties in pressure estimations from clinopyroxene crystals partly due to the higher analytical error of elements in low concentrations (e.g., $Na_2O \sim 4$–5%); therefore, such pressure-depth results should be treated with care (e.g., Wieser et al. 2022).

The feldspar chemistry shows larger variability between the lower and the top units compared to the more homogeneous clinopyroxene composition. Sanidine is the dominant K-feldspar phenocryst both in the lower and top units, with only a few crystals having anorthoclase composition in the lower unit (Fig. 6). The Ba and Sr content in the sanidine phenocrysts show only a minor variation in the lower unit (mainly below 1000 ppm), and a larger variation in the top unit having higher Ba values in average (Figs. 5, 6). Sanidine crystals in the top unit display normal zonation having higher Ba and Sr content in their core, reverse zonation with Ba-rich rims and step zonation with low-Ba core followed by a Ba-rich zone and a narrow rim with lower Ba content (Fig. 5). The change, or increase in Ba content can reflect a change in the melt composition, or temperature in case of sanidine phenocrysts (e.g., Ginibre et al. 2004; Troch et al. 2017). A mafic recharge causing the partial melting of the deeper cumulate phase could explain the rounded corners and the crystallization of Ba-rich rims of sanidine phenocrysts (e.g., Bachmann et al. 2014; Wolff et al. 2015; 2020; Ellis et al. 2023) leading to the reactivation of the system.

Plagioclase phenocrysts in the lower unit show homogeneous composition (An_{14}–An_{25}; Fig. 6) with no significant intra-crystalline variability, whereas in the top unit they show a larger variation in composition (An_{17}–An_{70}), with normal zonation in most of the cases. There is a strong positive correlation between the SrO and An content of the phenocrysts, whereas the FeO content shows only a slight correlation with the An content in the top unit (Fig. 6), implying only thermal (or H_2O) increase towards the parts with higher An content (e.g., Ginibre et al. 2002; Ginibre and Wörner 2007). The rims with higher An (and FeO, Sr) content might correspond to the increased heat transfer, which could have caused the reactivation of the system. The plagioclase of the crystal aggregates has a range of An_{20}–An_{48} overlapping with the phenocryst composition in both SrO and FeO content, implying that they originate from the same crystal mush zone of the volcanic plumbing system. In a few cases, rims with elevated FeO content occur (up to 0.8 wt%; Fig. 6), which are always in contact with clinopyroxene in the crystal aggregates. Elevated FeO content in plagioclase would reflect compositional mixing due to mafic magma recharge only if coupled with an increase in An content (e.g., Ginibre et al. 2002; Ginibre and Wörner 2007), which is not observed here. Alternatively, analytical artefacts can occur during the measurement of Fe in the vicinity of Fe-rich phases as it was previously noted by Ginibre and Wörner (2007). As these Fe-rich rims of plagioclase systematically occur here when in contact with clinopyroxene as part of the

crystal aggregate, this could be more plausible explanation than the magma mixing.

Crystallization temperatures were calculated from co-existing sanidine and plagioclase pairs using the two-feldspar calculation of Putirka (2008). This resulted in a uniform crystallization temperature of 786 ± 16 °C (standard deviation of $n = 22$ pairs, the uncertainty of the method is ca. 30 °C; Supplementary Material), with no difference between the lower and the top units. In only one case, the co-existing feldspar pair was part of a crystal aggregate containing clinopyroxene giving higher temperature of 914 ± 30 °C, which is in the range of crystallization temperatures calculated from the clinopyroxene composition.

Noble gas isotopic systematics in rhyolite

Noble gases in fluid inclusions, especially He, are very sensitive tracers of mantle (magmatic), crustal and atmospheric interactions (e.g., Hilton et al. 2002). It is a widely used method to track the origin of volatiles in different geodynamic settings (e.g., Ozima and Podosek 2004). Olivine, clino- and orthopyroxene, mantle xenoliths and mafic rocks are the main targets of the different studies (e.g., Martelli et al. 2004; Rizzo et al. 2015; Battaglia et al. 2018; Robidoux et al. 2020), whereas other mineral phases (e.g., amphibole, feldspar, garnet) and rock types (e.g., dacite) are less present (e.g., Hanyu and Kaneoka 1997; Correale et al. 2019; Molnár et al. 2021a; Álvarez-Valero et al. 2022). Here, we analyzed the He and Ne isotopic composition of clinopyroxene, sanidine and plagioclase of the older, lower (SG14) and younger, top (SG04) units to trace the evolution of volatiles within the volcanic plumbing system.

Regardless of the sampled unit, the clinopyroxene separates from the rhyolite revealed an almost pure crustal-derived fluid (> 99%) based on the He and Ne isotopic systematics having a relatively uniform R/R_a of ~ 0.04 R_a and $^4He/^{20}Ne$ ratios of 100–300 (Fig. 7). These $^4He/^{20}Ne$ ratios imply that these separates were not affected by atmospheric/meteoric water contamination allowing the preservation of their trapped signature. R/R_a ratios show slight differences, with lower values measured in the lower unit (~ 0.01 R_a). As this unit was more prone to suffer perlitic hydration, this difference could be caused by secondary processes, e.g., preferential ^3He loss relative to ^4He by diffusion (e.g., Dodson et al. 1997). This is also supported by its ^4He and ^{20}Ne content, which are in the same range as the top unit.

The contribution of the different reservoirs (mantle, crust and atmosphere) was calculated assuming a MORB end-member mantle value of 8 R_a (Graham 2002). The contribution of mantle fluids and volatiles at Šumovit Greben rhyolite would be < 1%, even if a metasomatized mantle is considered below the region, with a value of 3.1–4.5 R_a (as indicated by preliminary results of olivine phenocrysts from Mlado Nagoričane volcanic center; Fig. 1; Molnár et al. 2021b). These results are in line with the $^{143}Nd/^{144}Nd$ and $^{87}Sr/^{86}Sr$ isotopic ratios of the studied samples (0.512277–0.512382, 0.709208–0.709735, respectively; Molnár et al. 2022) implying crustal assimilation and fractional crystallization as the primary driving process in the evolution of the magmatic plumbing system beneath Šumovit Greben. Based on the noble gas systematics there is no evidence of pre-eruptive magma mixing with a more mafic melt, in agreement with the textural observations and geochemical characteristics. If mafic melts played any role before the eruptions that could have been manifested only in an increased heat transport. However, the volatiles possibly carried by these melts, were not trapped in the already crystallized phases. As there is no striking difference in the noble gas composition of the clinopyroxene separates from the bottom and top units, both represent earlier stage crystallized antecrysts, originating from the deeper part of the magma storage system. Only their proportions involved in the different erupted magmas differ.

Feldspar phenocrysts, especially sanidine crystals are less retentive than clinopyroxene with respect to noble gases, even at surface conditions (e.g., Lippolt and Weigel 1988). Both the plagioclase and the sanidine separates display lower noble gas concentrations than the clinopyroxene separates (Fig. 7). As their ^3He concentration is very close to the instrumental detection limit, calculating R/R_a ratios for these phases might be misleading and affected by high uncertainties. Their $^4He/^{20}Ne$ ratios show relatively uniform values of 3–6, implying a higher atmospheric/meteoric water contribution (~ 10%) than the clinopyroxene separates. However, their ^{20}Ne and especially ^4He content is an order of magnitude lower than in the clinopyroxene (Fig. 7), which crystallized earlier in the deeper part of the magmatic storage system. Thus, it is possible that either the trapped volatile content of plagioclase and sanidine was affected by magmatic degassing, or these phases lost their original volatile content during magma ascent (e.g., Dodson et al. 1997). Although some of the plagioclase crystallized together with clinopyroxene at an earlier stage, their contribution is much lower to the erupted materials and their possibly different composition is most likely obscured by to the large sample size (~ 1 g). Hence, neither the plagioclase nor the sanidine reflects the original volatile content of the evolving magma storage system and cannot be used as a direct indicator of primary magma storage processes.

The volcanic plumbing system and its relation to the Kožuf-Voras volcanic system

The petrological and geochemical features of the studied samples imply that the volcanic plumbing system beneath Šumovit Greben lava dome is composed of a deeper crystal mush, where mainly clinopyroxene, plagioclase and biotite

crystallized at approximately 900 °C characterized by a crustal-like noble gas signature of 0.04 R_a. A rhyolitic, crystal-poor lens developed as a result of melt extraction from this crystal mush zone, where additional plagioclase and sanidine crystallization took place at a lower temperature (ca. 790 °C; Fig. 10). Both the extrusive, lava dome building and explosive eruptions, which occurred between 2.89 and 2.77 Ma sampled mainly the overlying, crystal-poor lens. The last phase of volcanic activity, the extrusion

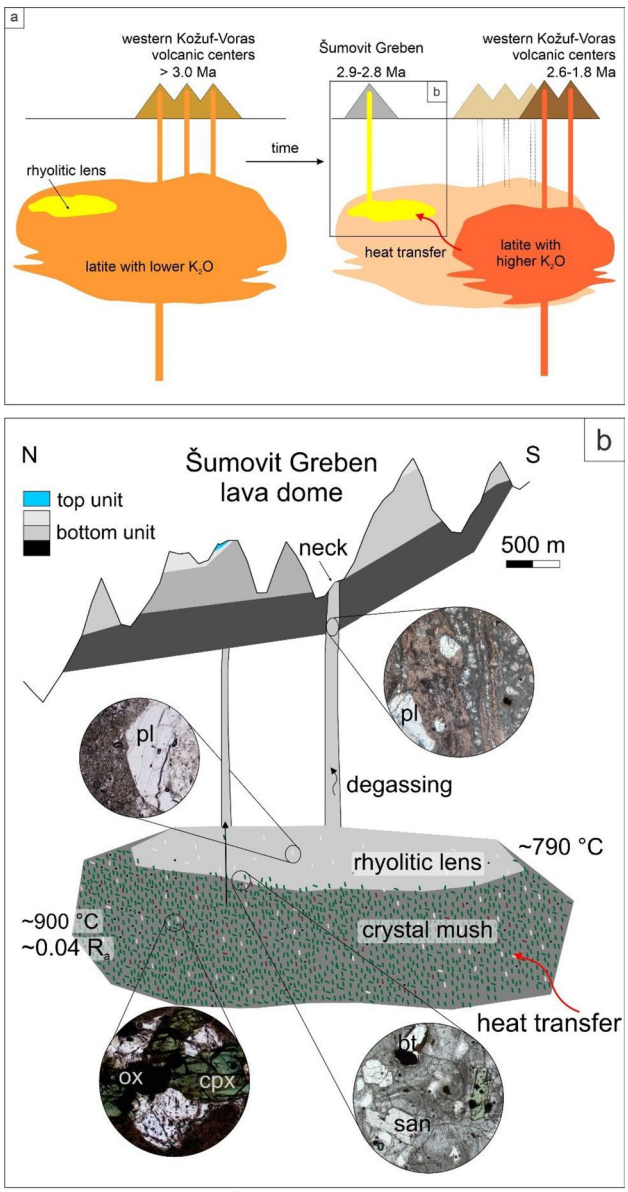

Fig. 10 **a** Possible relation of Šumovit Greben lava dome to the western part of the Kožuf-Voras volcanic system. Assumed melt compositions from the available whole-rock compositional data (Fig. 4). **b** Conceptual model of the magma plumbing system and storage conditions beneath Šumovit Greben lava dome Abbreviations on the petrographic photos: cpx: clinopyroxene, bt: biotite, san: sanidine, pl: plagioclase, ox: Fe–Ti oxide. Not to scale

of a small-volume lava flow, incorporated fragments from the deeper crystal mush zone, either contemporaneously with, or, shortly after the explosive eruption that deposited nearby a massive lapilli tuff layer. The plagioclase and clinopyroxene fractionation at depth resulted in low MgO (< 1 wt%) and Sr (< 300 ppm) content of the whole rock composition. The reactivation of the system after the main lava dome building phase could have occurred due to the implementation of mafic magma at depth causing heat transfer and partial cumulate melting in the system. This is supported by rounded corners and Ba-rich rims in the sanidine phenocrysts and spongy texture and elevated An and Sr content in the plagioclase rims occurring in the top unit.

Clinopyroxene is rare in cold-wet-oxidized rhyolites, but it is the main mafic phenocryst in the western part of the Kožuf-Voras volcanic system (group B and C in Figs. 4, 9). The eastern, older part, has amphibole as the dominant mafic phase (e.g., Boev and Yanev 2001; Eleftheriadis et al. 2003; group A in Figs. 4, 9). This can be the result of heterogeneity in the source region, formation of less hydrous magmas on the western side and/or different scale of crustal contamination during the magma evolution. The clinopyroxene ± plagioclase ± biotite glomeroporphyritic clots of Šumovit Greben lava dome, representing the deeper crystal mush zone, share similarities in the mineral composition with the nearby, more mafic lava domes located mainly along the Macedonian–Greek border (group C in Figs. 4, 9). These similarities and the close distance can imply that these lava domes might represent the silicic cumulate from which the rhyolitic lens has been formed by fractional crystallization and melt extraction, and they share a common, deeper part of the volcanic plumbing system (Fig. 10). The available eruption age data for the whole Kožuf-Voras volcanic system suggest that Šumovit Greben eruption occurred after an apparently longer quiescent period. Its activity was shortly followed by the eruption of more mafic magmas (with higher K_2O and lower SiO_2 content) forming the youngest lava domes (2.6–1.8 Ma, Kolios et al. 1980) in the southwestern part of the Kožuf-Voras volcanic system (Fig. 10). The (re) activation of the volcanic plumbing system beneath Šumovit Greben could be the result of thermal rejuvenation caused by the newly injected mafic magmas, which triggered the subsequent mafic eruptions (Fig. 10). Similar cycles (rejuvenation of a larger system starting with rhyolitic eruption) are found also elsewhere, e.g., in case of the Kos-Nisyros-Yali volcanic field in the nearby Aegean arc (Bachmann et al. 2019). The two thrust faults bounding Šumovit Greben and a presumed normal fault cutting through its structure (Fig. 2) could have acted as preferential pathways for the ascending magmas. Although the normal fault is covered by volcanics nowadays, it might have been active at ca. 3 Ma to drive the eruptions.

Conclusions

Mineral composition and whole-rock geochemical data were used to identify the volcanic plumbing system beneath the rhyolitic Šumovit Greben, the westernmost member of the Kožuf-Voras volcanic system. It consists of a deeper crystal mush of mainly clinopyroxene, biotite and plagioclase (i.e., silicic cumulate) and a shallower, crystal-poor rhyolitic lens containing primarily sanidine and plagioclase as phenocrysts. The crystallization temperature of the silicic cumulate was ca. 900 °C, whereas plagioclase and sanidine crystallized in the lens at a lower temperature (ca. 790 °C). The main lava dome of Šumovit Greben formed at ca. 2.9 Ma, which sampled exclusively the crystal-poor rhyolitic lens. After a short quiescence time, it was followed by an explosive eruption and the extrusion of a small-volume lava flow at ca. 2.8 Ma. The latter sampled the crystal-poor rhyolitic lens but also incorporated fragments of the deeper crystal mush as it contains abundant aggregates of clinopyroxene ± plagioclase ± biotite. The noble gas isotopic systematics from clinopyroxene fluid inclusions show an involvement of purely crust-derived fluids. The rejuvenation of the system was probably caused by a deeper mafic recharge causing heat transfer and partial melting of the cumulate, reflected by Ba-rich rims of the sanidine and An and Sr-rich rims of the plagioclase. Šumovit Greben might share a common deeper part with the nearby, more mafic volcanic centers of the Kožuf-Voras volcanic system. Based on their mineral composition and the available geochemical data, these more mafic lava domes might represent the same silicic cumulate from which the rhyolitic lens has been formed by fractional crystallization and melt extraction. The eruptions of Šumovit Greben could mark the start of the last cycle in the eruption history of Kožuf-Voras lasting from 2.9 to 1.8 Ma.

Supplementary Information The online version contains supplementary material available at https://doi.org/10.1007/s00410-023-02066-0.

Acknowledgements This research was supported by the European Union and the State of Hungary, financed by the European Regional and Development Fund in the project of GINOP-2.3.2-15-2016-00009 'ICER' project, co-financed by the French-Hungarian Cooperation Program TÉT-2018-00018 and TelluS 2020 program of INSU, CNRS. KM was supported by the Hungarian National Research, Development and Innovation Office within the OTKA PD project No. 135396. RA has received funding from the European Union's Horizon 2020 Research and Innovation Programme under grant agreement No. 101032448. Fieldwork was carried out under Research Permit No. UP1-11/1-1827/2019 issued by the Ministry of Environment and Physical Planning of the Republic of North Macedonia. The authors thank the help of Lajos Daróczi (University of Debrecen) for his assistance in SEM analyses and Alison Pereira (Université Paris-Saclay) for her help in Ar/Ar dating procedure. The SEM measurements at the Laboratory for Heritage Science were supported by the GINOP-2.3.3-15-2016-00029 'HSLab' project. The use of equipment in the Goettingen laboratory for correlative Light and Electron Microscopy (GoeLEM; www.mineralogie.uni-goettingen.de) is gratefully acknowledged. The authors thank Timothy L. Grove for the editorial handling of the manuscript and an anonymous reviewer for the constructive comments and suggestions.

Funding Open access funding provided by ELKH Institute for Nuclear Research.

Data availability All data obtained during this study are included in this published article and its supplementary file.

References

Álvarez-Valero AM, Sumino H, Burgess R et al (2022) Noble gas variation during partial crustal melting and magma ascent processes. Chem Geol 588:120635. https://doi.org/10.1016/j.chemgeo.2021.120635

Bachmann O, Bergantz GW (2008) Rhyolites and their source mushes across tectonic settings. J Petrol 49:2277–2285. https://doi.org/10.1093/petrology/egn068

Bachmann O, Miller CF, de Silva SL (2007) The volcanic–plutonic connection as a stage for understanding crustal magmatism. J Volcanol Geothermal Res 167:1–23. https://doi.org/10.1016/j.jvolgeores.2007.08.002

Bachmann O, Deering CD, Ruprecht JS et al (2012) Evolution of silicic magmas in the Kos-Nisyros volcanic center, Greece: a petrological cycle associated with caldera collapse. Contrib Miner Petrol 163:151–166. https://doi.org/10.1007/s00410-011-0663-y

Bachmann O, Deering CD, Lipman PW, Plummer C (2014) Building zoned ignimbrites by recycling silicic cumulates: insight from the 1,000 km3 Carpenter Ridge Tuff, Co. Contrib Mineral Petrol 167:1025. https://doi.org/10.1007/s00410-014-1025-3

Bachmann O, Allen SR, Bouvet de Maisonneuve C (2019) The Kos–Nisyros–Yali volcanic field. Elements 15:191–196. https://doi.org/10.2138/gselements.15.3.191

Battaglia A, Bitetto M, Aiuppa A et al (2018) The magmatic gas signature of Pacaya volcano, with implications for the volcanic CO2 flux from guatemala. Geochem Geophys Geosyst 19:667–692. https://doi.org/10.1002/2017GC007238

Boev B, Yanev Y (2001) Tertiary magmatism within the Republic of Macedonia: a review. Acta Vulcanol 13:57–71

Bullock LA, Gertisser R, O'Driscoll B (2018) Emplacement of the Rocche Rosse rhyolite lava flow (Lipari, Aeolian Islands). Bull Volcanol 80:48. https://doi.org/10.1007/s00445-018-1222-4

Burchfiel BC, Nakov R, Dumurdzanov N et al (2008) Evolution and dynamics of the Cenozoic tectonics of the South Balkan extensional system. Geosphere 4:919–938. https://doi.org/10.1130/GES00169.1

Carn SA, Pallister JS, Lara L et al (2009) The unexpected awakening of Chaitén Volcano, Chile. Eos Trans Amer Geophys Union 90:205–206. https://doi.org/10.1029/2009EO240001

Cashman K, Blundy J (2000) Degassing and crystallization of ascending andesite and dacite. Philos Trans R Soc Lond 358:1487–1513. https://doi.org/10.1098/rsta.2000.0600

Castro JM, Schipper CI, Mueller SP et al (2013) Storage and eruption of near-liquidus rhyolite magma at Cordón Caulle. Chile Bull Volcanol 75:702. https://doi.org/10.1007/s00445-013-0702-9

Correale A, Pelorosso B, Rizzo AL et al (2019) The nature of the West Antarctic Rift System as revealed by noble gases in mantle minerals. Chem Geol 524:104–118. https://doi.org/10.1016/j.chemgeo.2019.06.020

Cvetković V, Prelević D, Downes H et al (2004) Origin and geodynamic significance of Tertiary postcollisional basaltic magmatism in Serbia (central Balkan Peninsula). Lithos 73:161–186. https://doi.org/10.1016/j.lithos.2003.12.004

Deering CD, Bachmann O (2010) Trace element indicators of crystal accumulation in silicic igneous rocks. Earth Planet Sci Lett 297:324–331. https://doi.org/10.1016/J.EPSL.2010.06.034

Dodson A, Kennedy BM, DePaolo DJ (1997) Helium and neon isotopes in the Imnaha Basalt, Columbia River Basalt Group: evidence for a Yellowstone plume source. Earth Planet Sci Lett 150:443–451. https://doi.org/10.1016/S0012-821X(97)00090-3

Dumurdzanov N, Serafimovski T, Burchfiel BC (2005) Cenozoic tectonics of Macedonia and its relation to the South Balkan extensional regime. Geosphere 1:1–22. https://doi.org/10.1130/GES00006.1

Eleftheriadis G, Castorina F, Soldatos T, Masi U (2003) Geochemical and Sr–Nd isotopic evidence for the genesis of the Late Cainozoic Almopia volcanic rocks (Central Macedonia, Greece). Mineral Petrol 78:21–36. https://doi.org/10.1007/s00710-002-0217-0

Ellis BS, Wolff JA (2012) Complex storage of rhyolite in the central Snake River Plain. J Volcanol Geothermal Res 211–212:1–11. https://doi.org/10.1016/j.jvolgeores.2011.10.002

Ellis BS, Bachmann O, Wolff JA (2014) Cumulate fragments in silicic ignimbrites: the case of the Snake River Plain. Geology 42:431–434. https://doi.org/10.1130/G35399.1

Ellis BS, Wolff JA, Szymanowski D et al (2023) Cumulate recycling in igneous systems: the volcanic record. Lithos 456–457:107284. https://doi.org/10.1016/J.LITHOS.2023.107284

Fink JH (1983) Structure and emplacement of a rhyolitic obsidian flow: little glass mountain, medicine lake highland, northern California. GSA Bull 94:362–380. https://doi.org/10.1130/0016-7606(1983)94%3c362:SAEOAR%3e2.0.CO;2

Flinn D (1962) On folding during three-dimensional progressive deformation. Q J Geol Soc 118:385–428

Ginibre C, Wörner G (2007) Variable parent magmas and recharge regimes of the Parinacota magma system (N. Chile) revealed by Fe, Mg and Sr zoning in plagioclase. Lithos 98:118–140. https://doi.org/10.1016/j.lithos.2007.03.004

Ginibre C, Wörner G, Kronz A (2002) Minor- and trace-element zoning in plagioclase: implications for magma chamber processes at Parinacota volcano, northern Chile. Contrib Miner Petrol 143:300–315. https://doi.org/10.1007/s00410-002-0351-z

Ginibre C, Wörner G, Kronz A (2004) Structure and dynamics of the Laacher See Magma Chamber (Eifel, Germany) from major and trace Element Zoning in Sanidine: a Cathodoluminescence and electron microprobe study. J Petrol 45:2197–2223. https://doi.org/10.1093/petrology/egh053

Graham DW (2002) Noble gas isotope geochemistry of mid-ocean ridge and ocean island basalts: characterization of mantle source reservoirs. Rev Mineral Geochem 47:247–317. https://doi.org/10.2138/rmg.2002.47.8

Handy MR, Giese J, Schmid SM et al (2019) Coupled crust-mantle response to slab tearing, bending, and rollback along the Dinaride-Hellenide Orogen. Tectonics 38:2803–2828. https://doi.org/10.1029/2019TC005524

Hanyu T, Kaneoka I (1997) Magmatic processes revealed by noble gas signatures: the case of Unzen Volcano, Japan. Geochem J 31:395–405. https://doi.org/10.2343/geochemj.31.395

Higgins O, Sheldrake T, Caricchi L (2021) Machine learning thermobarometry and chemometry using amphibole and clinopyroxene: a window into the roots of an arc volcano (Mount Liamuiga, Saint Kitts). Contrib Miner Petrol 177:10. https://doi.org/10.1007/s00410-021-01874-6

Hildreth W (2007) Quaternary magmatism in the cascades—geological perspectives. US Geological Survey, Professional Papers 1744, p 125

Hildreth W, Fierstein J (2012) The Novarupta-Katmai eruption of 1912—largest eruption of the twentieth century; centennial perspectives. US Geol Surv Prof Pap 1791:259

Hilton DR, Fischer TP, Marty B (2002) Noble gases and volatile recycling at subduction zones. Rev Mineral Geochem 47:319–370. https://doi.org/10.2138/rmg.2002.47.9

Janković S, Boev B, Serafimovski T (1997) Magmatism and tertiary mineralization of the Kozuf metallogenetic district, the Republic of Macedonia with particular reference to the Alshar deposit. Štip, p 262

Kolios N, Innocenti F, Manetti P et al (1980) The pliocene volcanism of the Voras Mts (Central Macedonia, Greece). Bulletin Volcanologique 43:553–568. https://doi.org/10.1007/BF02597692

Lara LE (2009) The 2008 eruption of the Chaitén Volcano, Chile: a preliminary report. Andean Geology 36:125–129

le Bas MJ, le Maitre RW, Streckeisen A et al (1986) A chemical classification of volcanic rocks based on the total alkali-silica diagram. J Petrol 27:745–750. https://doi.org/10.1093/petrology/27.3.745

Lee J-Y, Marti K, Severinghaus JP et al (2006) A redetermination of the isotopic abundances of atmospheric Ar. Geochim Cosmochim Acta 70:4507–4512. https://doi.org/10.1016/j.gca.2006.06.1563

Lehmann St, Barcikowski J, von Quadt A et al (2013) Geochronology, geochemistry and isotope tracing of the Oligocene magmatism of the Buchim–Damjan–Borov Dol ore district: Implications for timing, duration and source of the magmatism. Lithos 180–181:216–233. https://doi.org/10.1016/j.lithos.2013.09.002

Lippolt HJ, Weigel E (1988) 4He diffusion in 40Ar-retentive minerals. Geochim Cosmochim Acta 52:1449–1458. https://doi.org/10.1016/0016-7037(88)90215-3

Ludwig KR (2012) User's manual for Isoplot version 3.75–4.15: a geochronological toolkit for Microsoft excel. Berkeley Geochronol Center Spec Publ 5:75

Manley CR, Fink JH (1987) Internal textures of rhyolite flows as revealed by research drilling. Geology 15:549–552. https://doi.org/10.1130/0091-7613(1987)15%3c549:ITORFA%3e2.0.CO;2

Martelli M, Nuccio PM, Stuart FM et al (2004) Helium–strontium isotope constraints on mantle evolution beneath the Roman Comagmatic Province, Italy. Earth Planet Sci Lett 224:295–308. https://doi.org/10.1016/j.epsl.2004.05.025

Molnár K, Czuppon G, Palcsu L et al (2021) Noble gas geochemistry of phenocrysts from the Ciomadul volcanic dome field (Eastern Carpathians). Lithos 394–395:106152. https://doi.org/10.1016/j.lithos.2021.106152

Molnár K, Temovski M, Palcsu L (2021b) First noble gas results from fluid inclusions of the Late Miocene-Pleistocene Macedonian volcanics. EGU General Assembly 2021 EGU21-9440

Molnár K, Lahitte P, Dibacto S et al (2022) The westernmost Late Miocene-Pliocene volcanic activity in the Vardar zone (North Macedonia). Int J Earth Sci 111:749–766. https://doi.org/10.1007/s00531-021-02153-2

Morimoto N, Fabries J, Ferguson AK et al (1988) Nomenclature of pyroxenes. Am Miner 73:1123–1133

Niespolo EM, Rutte D, Deino AL, Renne PR (2017) Intercalibration and age of the Alder Creek sanidine 40Ar/39Ar standard. Quat

Geochronol 39:205–213. https://doi.org/10.1016/j.quageo.2016.09.004
Ozima M, Podosek FA (2004) Noble gas geochemistry. Cambridge University Press
Pallister JS, Diefenbach AK, Burton WC et al (2013) The Chaitén rhyolite lava dome: eruption sequence, lava dome volumes, rapid effusion rates and source of the rhyolite magma. Andean Geol 40:277–294. https://doi.org/10.5027/andgeoV40n2-a06
Papp L, Palcsu L, Major Z et al (2012) A mass spectrometric line for tritium analysis of water and noble gas measurements from different water amounts in the range of microlitres and millilitres. Isotopes Environ Health Stud 48:494–511. https://doi.org/10.1080/10256016.2012.679935
Peccerillo A, Taylor SR (1976) Geochemistry of eocene calc-alkaline volcanic rocks from the Kastamonu area, Northern Turkey. Contrib Miner Petrol 58:63–81. https://doi.org/10.1007/BF00384745
Pouchou J-L, Pichoir F (1991) Quantitative analysis of homogeneous or stratified microvolumes applying the model "PAP." In: Heinrich KFJ, Newbury DE (eds) Electron probe quantitation. Springer US, Boston, pp 31–75
Putirka KD (2008) Thermometers and barometers for volcanic systems. Rev Mineral Geochem 69:61–120. https://doi.org/10.2138/rmg.2008.69.3
Ramsay DM (1979) Analysis of rotation of folds during progressive deformation. GSA Bull 90:732–738. https://doi.org/10.1130/0016-7606(1979)90%3c732:AOROFD%3e2.0.CO;2
Renne PR, Balco G, Ludwig KR et al (2011) Response to the comment by W.H. Schwarz et al on "Joint determination of 40K decay constants and 40Ar∗/40K for the Fish Canyon sanidine standard, and improved accuracy for 40Ar/39Ar geochronology" by P.R. Renne et al. (2010). Geochim Cosmochim Acta 75:5097–5100. https://doi.org/10.1016/j.gca.2011.06.021
Rizzo AL, Barberi F, Carapezza ML et al (2015) New mafic magma refilling a quiescent volcano: evidence from He-Ne-Ar isotopes during the 2011–2012 unrest at Santorini Greece. Geochem Geophys Geosyst 16:798–814. https://doi.org/10.1002/2014GC005653
Robidoux P, Rizzo AL, Aguilera F et al (2020) Petrological and noble gas features of Lascar and Lastarria volcanoes (Chile): inferences on plumbing systems and mantle characteristics. Lithos 370–371:105615. https://doi.org/10.1016/j.lithos.2020.105615
Sano Y, Marty B (1995) Origin of carbon in fumarolic gas from island arcs. Chem Geol 119:265–274. https://doi.org/10.1016/0009-2541(94)00097-R
Sano Y, Wakita H (1985) Geographical distribution of 3He/4He ratios in Japan: implications for arc tectonics and incipient magmatism. J Geophys Res Solid Earth 90:8729–8741. https://doi.org/10.1029/JB090iB10p08729
Sano Y, Marty B, Burnard P (2013) Noble gases in the atmosphere. In: Burnard P (ed) The noble gases as geochemical tracers. Springer Berlin Heidelberg, Heidelberg, pp 17–31
Schmid SM, Fügenschuh B, Kounov A et al (2020) Tectonic units of the Alpine collision zone between Eastern Alps and western Turkey. Gondwana Res 78:308–374. https://doi.org/10.1016/j.gr.2019.07.005
Sieh K, Bursik M (1986) Most recent eruption of the Mono Craters, eastern central California. J Geophys Res Solid Earth 91:12539–12571. https://doi.org/10.1029/JB091iB12p12539
Sun S-S, McDonough WF (1989) Chemical and isotopic systematics of oceanic basalts: implications for mantle composition and processes. Geol Soc Lon Spec Publ 42:313–345. https://doi.org/10.1144/GSL.SP.1989.042.01.19
Szepesi J, Lukács R, Soós I et al (2019) Telkibánya lava domes: Lithofacies architecture of a Miocene rhyolite field (Tokaj Mountains, Carpathian-Pannonian region, Hungary). J Volcanol Geotherm Res 385:179–197. https://doi.org/10.1016/j.jvolgeores.2019.07.002
Troch J, Ellis BS, Mark DF et al (2017) Rhyolite generation prior to a Yellowstone supereruption: insights from the Island Park-Mount Jackson Rhyolite series. J Petrol 58:29–52. https://doi.org/10.1093/petrology/egw071
Vermeesch P (2012) On the visualisation of detrital age distributions. Chem Geol 312–313:190–194. https://doi.org/10.1016/j.chemgeo.2012.04.021
Vougioukalakis G (1994) The Pliocene volcanites of the Voras mountain, Central Macedonia, Greece. Bull Geol Soc Greece 30:223–240
Wieser P, Kent A, Till CB, et al (2022) Barometers behaving badly: Assessing analytical and experimental error on clinopyroxene thermobarometry. 2022 Goldschmidt Conference
Wolff JA, Ellis BS, Ramos FC et al (2015) Remelting of cumulates as a process for producing chemical zoning in silicic tuffs: a comparison of cool, wet and hot, dry rhyolitic magma systems. Lithos 236–237:275–286. https://doi.org/10.1016/J.LITHOS.2015.09.002
Wolff JA, Forni F, Ellis BS, Szymanowski D (2020) Europium and barium enrichments in compositionally zoned felsic tuffs: a smoking gun for the origin of chemical and physical gradients by cumulate melting. Earth Planet Sci Lett 540:116251. https://doi.org/10.1016/J.EPSL.2020.116251
Yanev Y, Boev B, Doglioni C et al (2008) Late Miocene to Pleistocene potassic volcanism in the Republic of Macedonia. Mineral Petrol 94:45–60. https://doi.org/10.1007/s00710-008-0009-2